Geophysical Journal International

Geophys. J. Int. (2012) **190,** 1123–1134 doi: 10.1111/j.1365-246X.2012.05528.x

Roles of quartz and mica in seismic anisotropy of mylonites

Dustin Ward, Kevin Mahan and Vera Schulte-Pelkum

Department of Geological Sciences, University of Colorado, Boulder, CO, USA. E-mail: dustin.ward@colorado.edu

Accepted 2012 April 27. Received 2012 April 26; in original form 2011 September 24

SUMMARY

Observations of seismic anisotropy in continental crust are of primary importance to understanding deep crustal structure and dynamics. While many crustal minerals are elastically anisotropic, seismic studies commonly assume that only the most anisotropic minerals (e.g. micas) are responsible for the observed anisotropic signal while making the simplifying assumption that potential interaction of multiple mineral phases is insignificant. This study explores the interference effects between mica and quartz on the calculated response of compressional and shear waves in high-strain tectonites (mylonites). Sample texture and mineralogy were evaluated via electron backscatter diffraction and the calculation of seismic response was carried out over a range of mica to quartz ratios. Both natural and synthetic crystallographic orientation data, which mimic quartz and mica orientations under increasing temperature in high, non-coaxial strain settings, were evaluated. Not surprisingly, the results show that adding quartz to micaceous lithologies significantly reduces the magnitude of seismic anisotropy. However, the study also highlights the mutually destructive nature of this relationship and suggests a critical threshold proportion between the two phases across which the symmetry of the end-member induced anisotropies becomes significantly altered, a result that may have significant implications for studies interpreting crustal dynamics from seismic anisotropy.

Key words: Microstructures; Seismic anisotropy; High strain deformation zones; Crustal structure.

INTRODUCTION

Seismic anisotropy studies are taking on increasingly important roles in characterization of middle and lower continental crustal structure. Teleseismic receiver function analyses detect *P*- and *S*-velocity anisotropy (e.g. Sierra Nevada and southern California, western U.S., Zandt *et al.* 2004 and Porter *et al.* 2011; Himalayan–Tibetan orogen, Schulte-Pelkum *et al.* 2005; Northern Apennines, Italy, Roselli *et al.* 2010). Surface wave analyses from both earthquake (e.g. Himalayan–Tibetan orogen, Shapiro *et al.* 2004) and ambient noise sources (e.g. Himalayan–Tibetan orogen, Huang *et al.* 2010; western U.S., Moschetti *et al.* 2010) are sensitive to shear velocity anisotropy. Shear wave splitting studies in the crust typically focus on shallow anisotropy due to cracks in the brittle upper crust using local earthquakes, although there have been attempts to measure deeper crustal shear velocity anisotropy using splitting in converted teleseismic phases (McNamara & Owens 1993; Peng & Humphreys 1997).

Key contributors to deep crustal seismic anisotropy include mineralogy and the degree of deformation-induced alignment (crystallographic preferred orientation or CPO) among anisotropic phases (e.g. Mainprice & Nicolas 1989). Most common crustal minerals are seismically anisotropic (Ji *et al.* 2002), but mica is the most anisotropic mineral group and tends to align with its seismically fast plane in the foliation planes of deformed rocks. Thus, crustal studies commonly assume that mica is the sole contributor to observed anisotropy (e.g. Rey *et al.* 1994; Shapiro *et al.* 2004; Huang *et al.* 2010; Porter *et al.* 2011). While the contribution of phases other than mica have also been studied in some detail (e.g. quartz, Mainprice & Casey 1990; Lloyd & Kendall 2005; Lloyd *et al.* 2010; calcite, Khazanehdari *et al.* 1998; hornblende, Tatham *et al.* 2008), relatively few attempts have been made to explore the detailed interactions or interference effects between multiple mineral phases (Meissner *et al.* 2006; Lloyd *et al.* 2011a,b). Lloyd *et al.* (2009) investigated the anisotropic role of multiple fabric components in composite *S*–*C* mylonites.

Here, an attempt to explore the precise interference effects between mica and quartz in high-strain shear zone tectonites focuses primarily on the calculated seismic response of three quartz- and mica-bearing mylonites. Textural analysis via electron backscatter diffraction (EBSD) allows characterization of the mineralogy and deformation fabric of each sample. A combination of crystallographic orientation data and elastic properties for quartz, muscovite and biotite, were used to calculate velocity anisotropy using the AnisCh5 software of Mainprice (1990). Compressional (AV_p) or shear wave anisotropy (AV_s1 for fast shear wave) are calculated as $[(V_{\max} - V_{\min})/[(V_{\max} + V_{\min})0.5]]*100$, where V is V_p or V_s1, respectively. An alternative form for shear wave anisotropy is per cent splitting (AV_s) as $[(V_s1 - V_s2)/[(V_s1 + V_s2)0.5]]*100$, where V_s1 and V_s2 are the fast and slow shear wave velocities, respectively. These properties were also calculated over a range of quartz to mica ratios, a strategy similar to that of Tatham *et al.* (2008), Lloyd *et al.*

(2009) and Naus-Thijssen *et al.* (2011). The results are compared to the calculated seismic response of synthetic data sets that mimic common quartz and mica CPO patterns for high-strain tectonites as a function of increasing temperature (Schmid & Casey 1986). While the broadly diluting effect of quartz on mica-induced anisotropy is not in itself surprising (e.g. Ji *et al.* 1993; Naus-Thijssen *et al.* 2011), the results also suggest several other features that may be important in future crustal anisotropy studies. These include the mutually destructive nature of mica and quartz for low to moderate temperature deformation conditions and the suggestion of a critical threshold proportion between the two phases across which the symmetry of the end-member induced anisotropies becomes significantly altered.

SAMPLE DESCRIPTION, EBSD METHODS AND MINERAL CPO

Three quartz-rich mylonites (two quartzites, one amphibolite) were collected from separate shear zones with varying metamorphic grade. All samples are believed to have developed under general shear conditions with a strong simple shear component based on the presence of well-developed asymmetric shear sense indicators and previous field-based studies of the shear zone locations. Each sample was selected to capture activity on the most common quartz slip systems active under greenschist, lower amphibolite and upper amphibolite facies conditions (Schmid & Casey 1986; Passchier & Trouw 2005). Samples were studied in thin sections cut parallel to lineation and perpendicular to foliation (e.g. a standard kinematic plane or *XZ* section where *Z* is perpendicular to the mylonitic *C*-plane). Quartz grains in all samples are completely recrystallized and range in size from 10 to 100 μm. Therefore, examination of quartz CPO's in XZ sections alone likely provides a sufficient evaluation of overall quartz orientation data for the purpose of this study (*cf*. Lloyd *et al.* 2010). EBSD data were collected from representative areas greater than several square millimetres. All samples exhibit composite fabrics (*S–C* or *C*') with asymmetry consistent with the shear sense observed in their respective shear zones (oriented as dextral in this study).

EBSD analysis methods

Each sample underwent a minimum of 1 hr, maximum of 2 hr of chemical/mechanical polishing using Buehler's MasterMet two non-crystallizing colloidal silica polishing suspension and Chemomet I polishing cloth. For samples CB-q and GR-a, a thin (<10 nm) layer of carbon was applied to dissipate charge build-up during data collection; the low-vacuum mode for analysis of sample ISR-q negated the requirement for a conductive coating. EBSD data were collected on sample CB-q using an FEI Nova 600i SEM with an EDAX-TSL EBSD attachment (University of Colorado-Boulder). Data for samples ISR-q and GR-a were collected with an Oxford Instruments HKL EBSD system using a JEOL JSM 6480LV SEM and a 5800LV SEM, respectively (the former at the University of Colorado-Boulder and the latter at the University of Wyoming). Phase and orientation data were mapped over 1.5–2.5 mm^2 areas with 5–9 μm step sizes. Operating conditions included a 20 kV accelerating voltage, 11–14 mm working distances, and a 70° stage tilt. The overall indexing rates were 85–90 per cent for the quartzites and approximately 50 per cent for the amphibolite with a maximum acceptable MAD value (mean angular deviation) of 1.0°. Properly indexing phyllosilicate minerals using EBSD can be challenging and additional care was taken to ensure data quality by cross checking against optical observations from the samples.

Quartzite mylonites: samples CB-q and ISR-q

All three samples were collected from the high-strain core regions of kilometres-scale Palaeoproterozoic shear zones. Sample CB-q (Fig. 1a) is a mylonitic quartzite from the northern strand of the

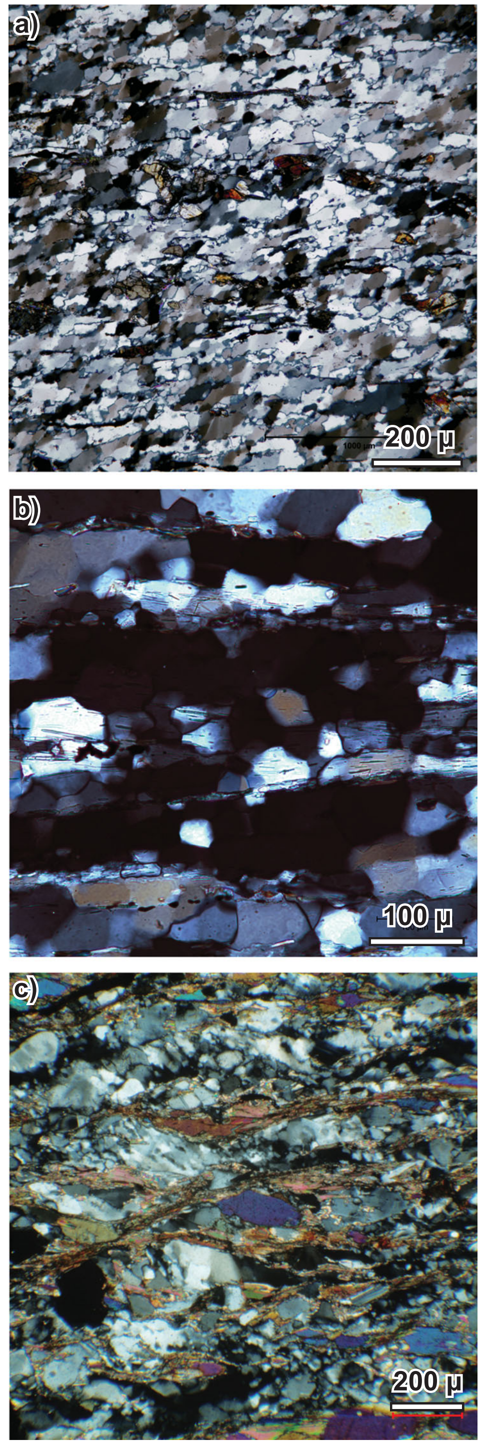

Figure 1. (a) Cross polarized light photomicrograph of quartzite sample CB-q, (b) Cross polarized light photomicrograph of quartzite sample ISR-q and (c) Cross polarized light photomicrograph of amphibolite sample GR-a.

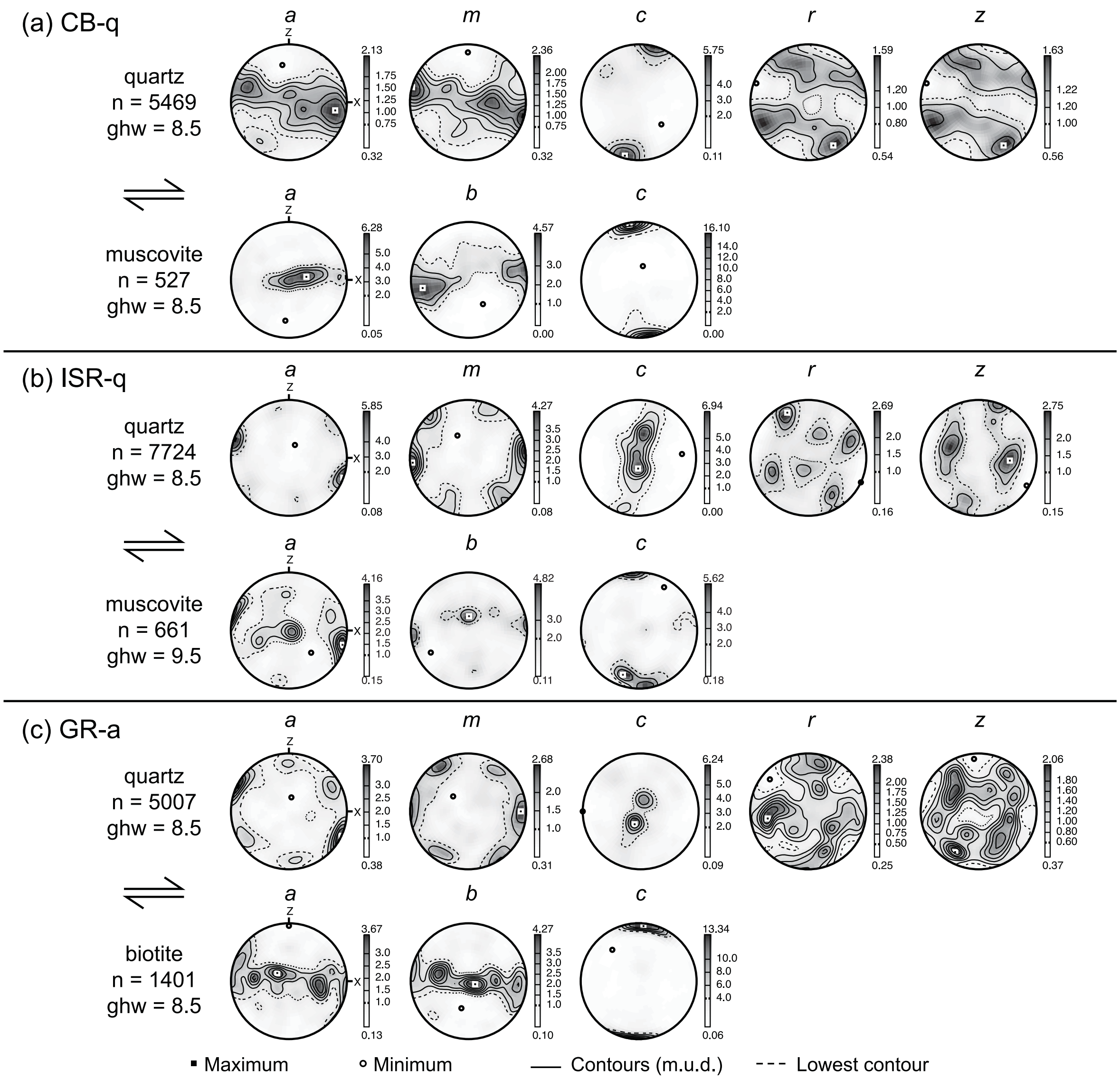

Figure 2. Equal area, lower hemisphere, stereographic projections of quartz *a, m, c, r* and *z* orientations and mica *a, b* and *c* orientations for samples (a) CB-q, (b) ISR-q and (c) GR-a. All pole figures represent *x–z* structural planes. ghw, Gaussian half-width.

Cheyenne Belt in southern Wyoming (Mullen Creek-Nash Fork shear zone). This shear zone is the suture between the Archean Wyoming craton and Proterozoic arc terranes of the southwestern U.S. (e.g. Karlstrom & Houston 1984; Chamberlain *et al.* 2003). This sample contains ∼95 per cent quartz, ∼3 per cent muscovite and ∼2 per cent kyanite. Duebendorfer (1988) reports temperature–pressure conditions for this region of 475 °C and 0.37–0.44 GPa, consistent with kyanite stability. Sample ISR-q (Fig. 1b) is from mylonitized Coal Creek quartzite in the Idaho Springs-Ralston shear zone northwest of Golden, Colorado, a structure associated with early continental assembly and Mesoproterozoic intracontinental deformation of the southwestern U.S. (McCoy *et al.* 2005). Modal mineralogy is ∼95 per cent quartz, ∼3 per cent muscovite and ∼2 per cent sillimanite. Peak metamorphic conditions of mylonitization are estimated to between 500 and 600 °C and near 0.4 GPa based on mineral assemblages in associated pelitic units (e.g. kyanite ≥ andalusite ≥ sillimanite) and quartz and feldspar microstructures in associated mylonitic granitoid units (McCoy *et al.* 2005).

In both quartzite samples, *S–C* fabrics are defined by quartz grain shape and aligned muscovite. Quartz grains in sample CB-q exhibit irregular, ‘bulging’ grain boundaries and distinct internal subgrains indicating that grain boundary migration and subgrain rotation were the dominant recrystallization mechanisms, generally consistent with regime-2 deformation of Hirth & Tullis (1992). Quartz grain boundaries in sample ISR-q also suggest grain boundary migration and subgrain rotation recrystallization. However, many quartz grains fully encapsulate muscovite and sillimanite grains indicating a higher degree of grain boundary mobility during recrystallization of this sample than in sample CB-q and appear transitional between regime-2 and regime-3 of Hirth & Tullis (1992). Mica stability in both quartzite samples suggests a grain boundary fluid was probably present during deformation.

Quartz orientation data for sample CB-q (Fig. 2a) suggest basal <*a*>, and to a lesser extent, rhombohedral <*a*> were the dominant slip systems during deformation. Quartz orientation data for sample ISR-q (Fig. 2b) reveal basal <*a*>, rhombohedral <*a*> and prism <*a*> were active slip systems during deformation. For ISR-q, the resulting quartz *c*-axes form a single girdle similar to sample CC1 of Schmid & Casey (1986) and Mainprice & Casey (1990). Concentrations of muscovite *c*-axes slightly counter-clockwise of the *X–Y* plane (*C* foliation plane) are interpreted to reflect alignment in both *S* and *C* foliation planes. Although we do not explicitly treat *S* and *C* plane mica alignment separately (Lloyd *et al.* 2009), the effect of these composite fabrics is captured in the full EBSD data sets.

Grease River shear zone garnet-amphibolite: sample GR-a

Sample GR-a (Fig. 1c) is from the Grease River shear zone in the Churchill province of the western Canadian Shield (Mahan & Williams 2005; Dumond *et al.* 2008). Deformation in this strike-slip shear zone initiated under high-pressure granulite-facies conditions (Dumond *et al.* 2008) but evolved to mid-crustal amphibolite- and greenschist-facies conditions during exhumation of the larger host Athabasca Granulite Terrane (Mahan & Williams 2005; Mahan 2006). Pressure and temperature conditions of other similar mid-crustal shear zones in the region are estimated at 550–650 °C and 0.5–0.4 GPa (Mahan *et al.* 2006), which are consistent with the mineral assemblage in this sample. The sample contains 27 per cent quartz and 8 per cent biotite as well as hornblende, plagioclase, garnet and minor ilmenite. The mylonitic *C–C*' foliation is defined by biotite, hornblende and a shape-preferred orientation of quartz and feldspar. The calculated anisotropy is not meant to be realistic for this specific sample due to the exclusion of the additional phases in the mineral assemblage (only quartz and biotite are considered), but rather, the intention is simply to explore the general case of an additional degree of variation in quartz CPO versus mica at higher temperature than the two quartzite samples.

Quartz orientation data for sample GR-a (Fig. 2c) suggest prism <*a*> slip was the dominant slip system during deformation. The quartz *c*-axes form a *y*-axis maximum, similar to sample P248 of Schmid & Casey (1986) and Mainprice & Casey (1990). A concentration of biotite *c*-axes slightly clockwise of the *X–Y* plane reflects the combined alignment of biotite in both *C* and *C*' foliation planes.

ANALYSIS AND DISCUSSION

Single crystal properties

Single crystal velocity properties of muscovite, biotite and quartz (McSkimin *et al.* 1965; Aleksandrov *et al.* 1974; Vaughan & Guggenheim 1986) are shown in Fig. 3. Micas exhibit the highest compressional wave velocities and the greatest degree of shear wave splitting within the crystallographic *a-b* plane. The slowest compressional wave velocities and the minimum difference in shear wave velocities in micas occur parallel to the crystallographic *c*-axis. This holds true for both biotite and muscovite, though the magnitude of AV_p and maximum AV_s is greater in biotite. Quartz has three compressional wave maxima and three minima, which are subparallel to the *z*- and *r*-directions, respectively. Shear wave splitting in quartz is complex, with minimum velocity anisotropy subparallel to the *r*-directions and maximum velocity anisotropy occurring subparallel to the *a*-axes and at intermediate angles between the *c*-axis and *r*-directions.

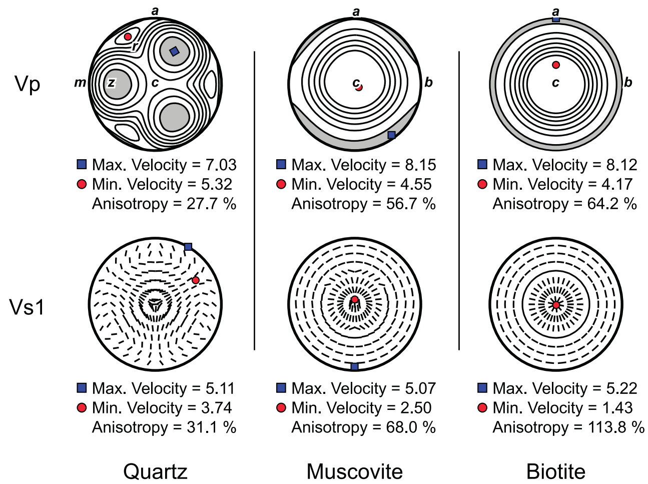

Figure 3. Stereographic projection of the calculated V_p and V_s1 (the fast shear wave) of single crystal quartz, muscovite and biotite. Shear wave anisotropy listed is that of the fast shear wave (AV_s1).

Anisotropy of muscovite-quartz aggregates

The relationships between quartz deformation and metamorphic conditions are understood well enough that predictable quartz CPO patterns can be recognized with increasing temperature (e.g. Lister 1977; Schmid & Casey 1986). As seismic anisotropy is dictated in large part by the degree of crystallographic alignment among anisotropic phases, deformation by dislocation creep of quartz should result in an increase in the anisotropy magnitude generated by this phase (e.g. Mainprice & Casey 1990). However, the combined interference effects due to the presence of both aligned quartz and mica and its influence on seismic anisotropy are not well understood. For example, McDonough & Fountain (1993) suggest quartz exhibits a significant influence on seismic anisotropy in their study while Rey *et al.* (1994) assume quartz imparts no influence on bulk seismic anisotropy despite a strong CPO. Ji *et al.* (1993) report quartz as having an anisotropy that cancels with other phases (i.e. feldspars). Lloyd *et al.* (2010) examine the seismic anisotropy produced solely by quartz, while intentionally excluding small amounts of aligned mica.

The seismic response of each sample was calculated using the EBSD-derived CPO of quartz and mica [elastic tensors for each calculation provided in Supporting Information]. Additionally, synthetic data (5000 manually compiled Euler angle triplets for each CPO pattern) were generated to mimic common quartz crystallographic orientations occurring under increasing temperature in high non-coaxial strain settings (Fig. 4). Seismic calculations were carried out for both the synthetic and natural data sets over simulated compositions ranging from 100 per cent mica to 100 per cent quartz. For simplicity, quartz and mica are the only phases considered. Naus-Thijssen *et al.* (2011) performed similar calculations but considered only single-crystal orientations for quartz rather than natural CPO patterns. We used the approach of Mainprice (1990) and Mainprice & Humbert (1994) and report the Voigt-Reuss-Hill average. Other calculation methods such as asymptotic expansion homogenization may ultimately serve to better account for grain–scale interactions (Naus-Thijssen *et al.* 2011).

Calculations for each sample were performed using quartz to mica ratios that reflect sample modal proportions and for the full range of hypothetical modal proportions (Fig. 5). Quartzite samples CB-q and ISR-q have high quartz to mica ratios with normalized

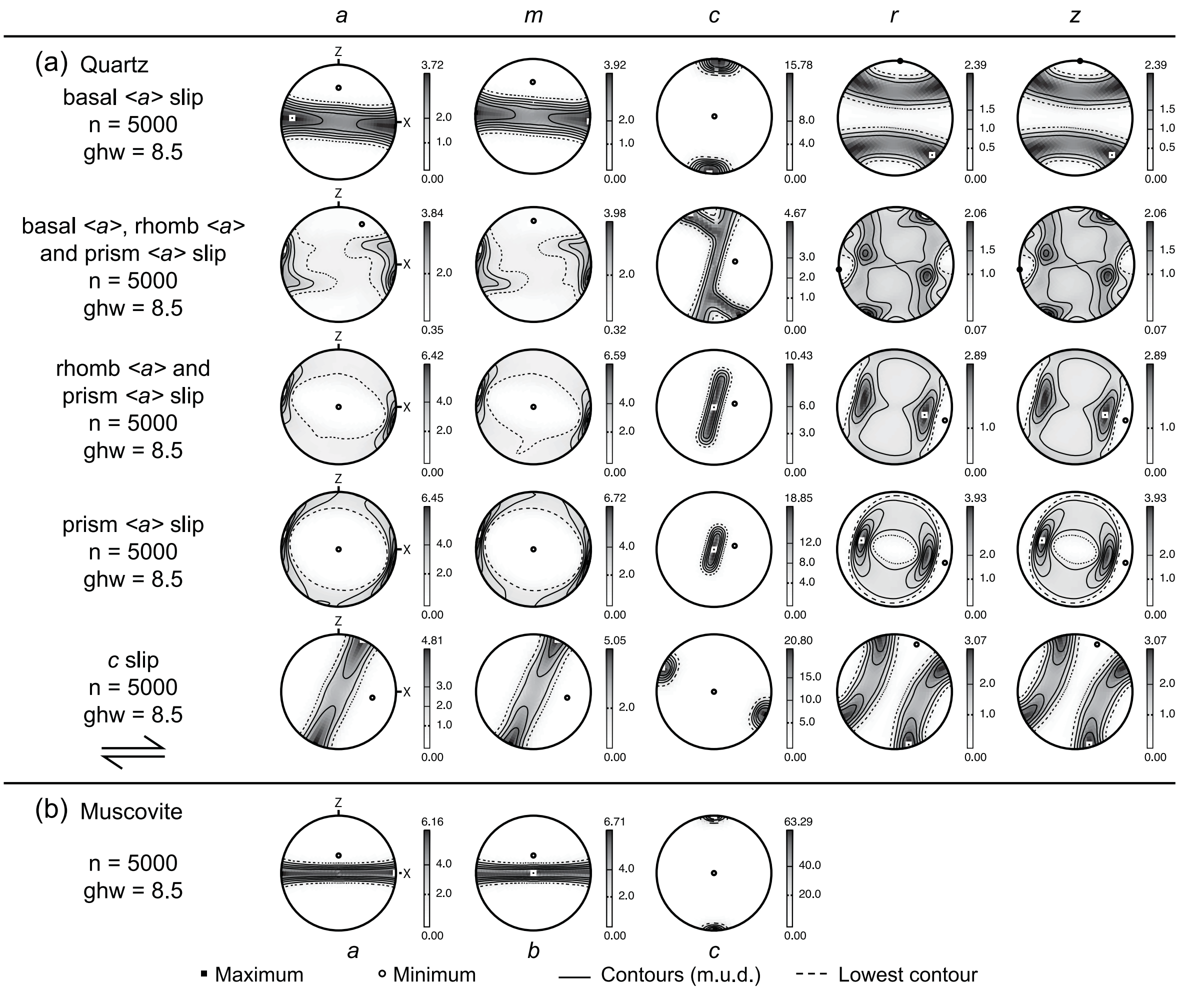

Figure 4. Equal area, lower hemisphere, stereographic projections of quartz *a, m, c, r* and *z* orientations and mica *a, b* and *c* orientations of synthetically generated data sets. CPO patterns are representative of commonly occurring patterns developing under non-coaxial progressive deformation and increasing metamorphic grade. ghw, Gaussian half-width. All pole figures represent *x–z* structural planes.

proportions of 97.5 per cent quartz, 2.5 per cent muscovite and 97.6 per cent quartz, 2.4 per cent muscovite, respectively. Sample GR-a normalizes to 78.1 per cent quartz and 21.9 per cent biotite.

All calculations using natural sample orientation data show the highest magnitude of AV_p and AV_s occurs in high mica simulations. At compositions of 100 per cent mica AV_p is 37 per cent, 14 per cent and 31 per cent and maximum AV_s is 36 per cent, 18 per cent and 45 per cent for samples CB-q, ISR-q and GR-a, respectively (Figs 5 and 6). Note that this is significantly less than mica single crystal anisotropies (Fig. 3) due to variation of the crystallographic orientation of constituent mica grains. Sample ISR-q shows the highest degree of spread in mica CPO due to alignment of this phase in both the *S* and *C* planes, which is likely the reason this sample exhibits lower anisotropy magnitude than the other samples in which micas only weakly align in the *S* plane. The effect of mica-alignment in composite shear fabrics was investigated explicitly by Lloyd *et al.* (2009).

On the other end of the spectrum, anisotropies at 100 per cent quartz compositions are 7 per cent, 10 per cent and 7 per cent AV_p and 9 per cent, 11 per cent and 8 per cent maximum AV_s for sample in CB-q, ISR-q and GR-a, respectively, which are comparable to previous studies of anisotropy in quartzites (Mainprice & Casey 1990; Lloyd & Kendall 2005; Lloyd *et al.* 2010). The fact that overall anisotropies are lower in quartz-rich calculations is not surprising given the considerable difference in quartz and mica elastic properties. However, the lowest magnitude of AV_p and lowest maximum AV_s do not occur at a composition of 100 per cent quartz as may be expected (Figs 5b and 6b). The addition of quartz to mica rich compositions diminishes the magnitude of both AV_p and maximum AV_s to a threshold composition. Beyond this composition (with continued increase in quartz–mica ratio), anisotropy magnitudes increase again. The minimum AV_p magnitude occurs between approximately 70 per cent (ISR-q) and 96 per cent quartz (GR-a). Again, the weaker alignment of micas is a likely explanation for the position of this minimum in sample ISR-q, which is at a lower quartz composition than the other samples. Similar observations of a minimum in AV_p magnitude that occur between 82 and 100 per cent quartz were made by Naus-Thijssen *et al.* (2011) using single crystal quartz orientations.

Similar patterns are observed from calculations with synthetic crystallographic orientation data. The highest degree of AV_p, 54.9 per cent, and maximum AV_s, 65 per cent occurs in 100 per cent mica calculations (Figs 7 and 8). Compositions of 100 per cent quartz produce AV_p values ranging from 9 to 13 per cent, and maximum AV_s values from 6 to 16 per cent, depending upon

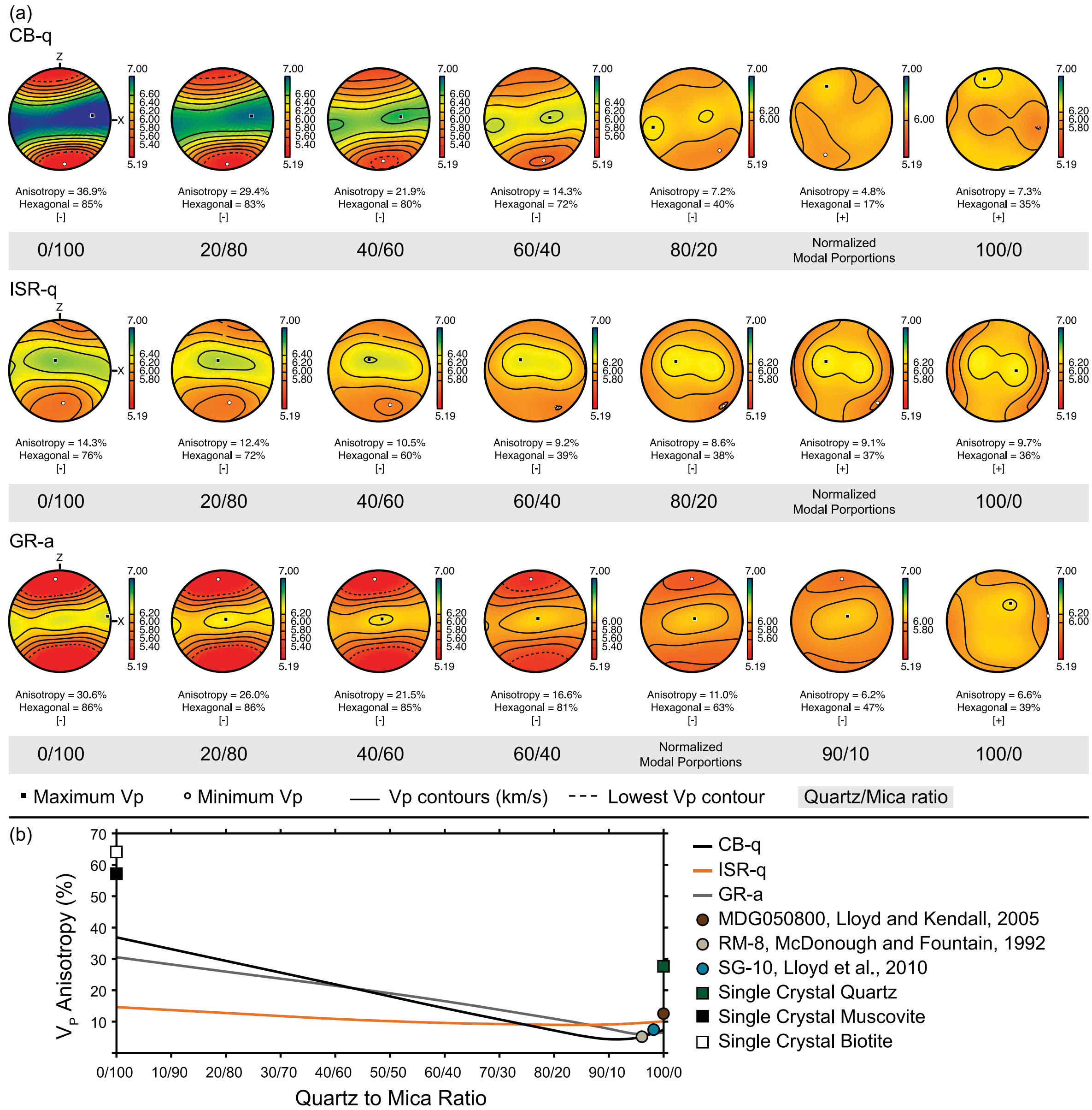

Figure 5. (a) Equal area, lower hemisphere stereographic projections of V_p calculated for a range of quartz to mica ratios varying from 100 per cent mica to 100 per cent quartz using orientation data from CB quartzite, ISR quartzite and GR amphibolite. Contours are km s^{-1}. Pole figures represent *x–z* structural planes. Percentage anisotropy was calculated with AnisCh5 (Mainprice 1990); percentage hexagonal is the proportion of the total tensor anisotropy that has hexagonal symmetry as calculated with code of Browaeys & Chevrot (2004). The sign indicates slow (negative) or fast (positive) symmetry axis. (b) AV_p variation with increasing quartz content for samples CB-q, ISR-q and GR-a. Circles show composition and AV_p for samples MD of Lloyd & Kendall (2005), RM-8 of McDonough & Fountain (1993), and SG-10 of Lloyd *et al.* (2010). Squares show single crystal AV_p of quartz, muscovite, and biotite from Ji *et al.* (2002).

active quartz slip systems and the resulting quartz CPO. The lowest calculated AV_p and maximum AV_s values increase in magnitude and shift to higher quartz compositions (from 84 per cent quartz up to 100 per cent quartz) with increasing temperature slip system combinations.

The compositional location and the magnitude of the anisotropy minima appear to be dictated by the degree of alignment between the seismically fast axes in micas (the *a* and *b* axes) and the fast directions (the *z*-directions) in quartz. For example, for the lowest temperature quartz CPO patterns, basal <*a*> slip aligns the *z*-directions in quartz and mica *a* and *b* axes into girdles that trend subparallel to but not coincident with one another (Fig 2). This scenario results in minimal overlap between the fast plane in micas and the fast directions in quartz and thus produces the greatest amount of destructive interference. As temperature increases, different quartz slip systems become active resulting in greater overlap between the fast *z*-directions and mica *a–b* planes and less destructive interference between these phases. At high temperature alpha-quartz transitions to beta-quartz (approximately 573 °C at atmospheric pressure and 820 °C at 1.0 GPa; Deer *et al.* 1992), which exhibits significantly lower seismic anisotropy (Mainprice & Casey 1990). Thus, in some granulite-facies environments where beta-quartz may be the stable SiO_2 polymorph, the resulting CPO from *c*-slip in quartz may produce very low anisotropy.

Another important observation among all calculations is that the symmetries of V_p and V_s splitting are significantly altered across

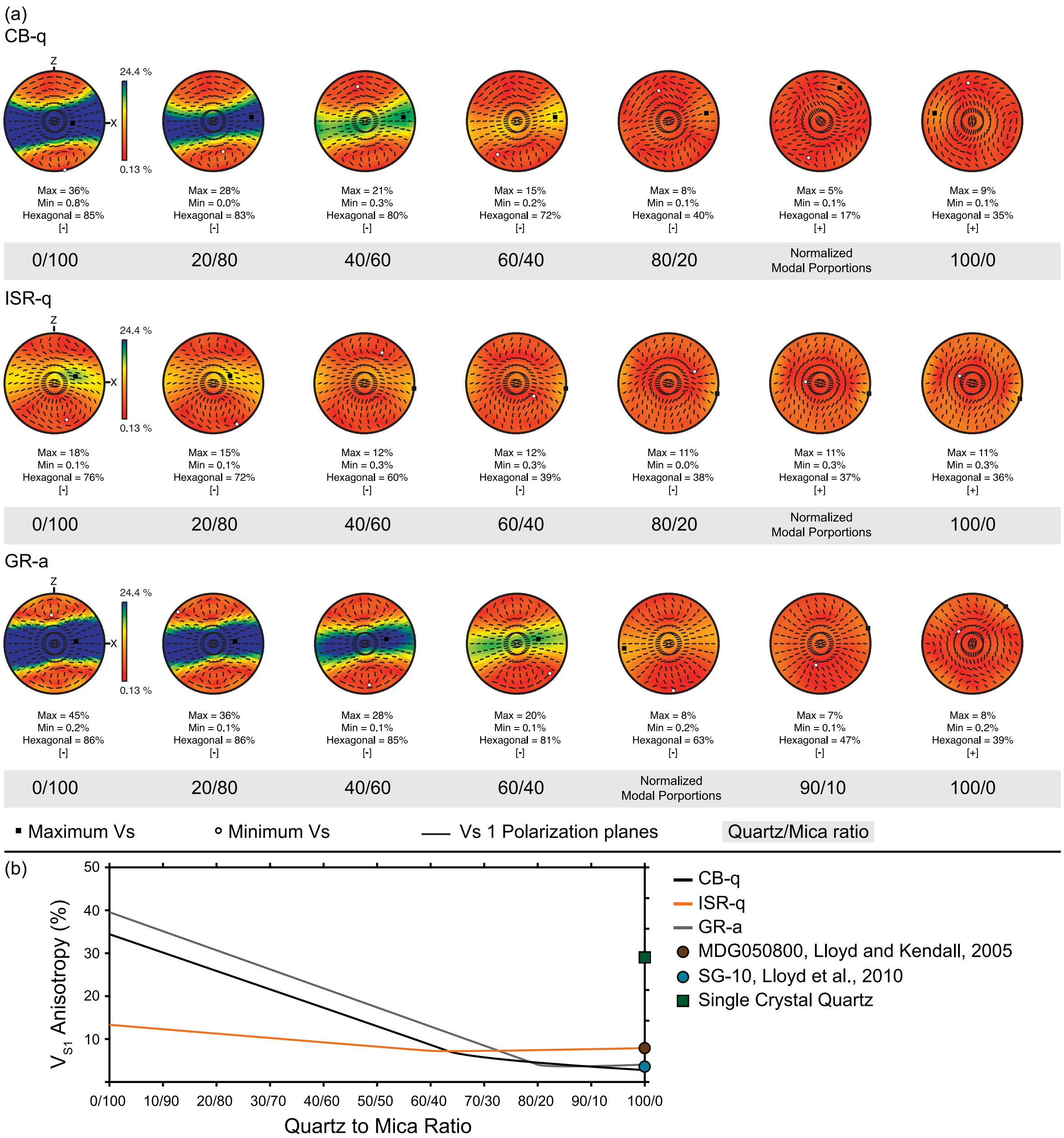

Figure 6. (a) Equal area, lower hemisphere stereographic projections of AV_s (per cent splitting) calculated for a range of quartz to mica ratios for samples CB-q, ISR-q and GR-a. Dashed lines represent the trace of V_s1 polarization planes. (b) Variation of velocity anisotropy of the fast shear wave (AV_s1) with increasing quartz content. Circles show composition and AV_s1 anisotropy from sample MD of Lloyd & Kendall (2005), and SG-10 of Lloyd *et al.* (2010).

a threshold compositional proportion. For this discussion, we use the proportions of hexagonal versus lower symmetry classes (e.g. orthorhombic, triclinic, etc.) as calculated using the tensor decomposition code of Browaeys & Chevrot (2004). This code determines what percentage of the norm of the elasticity tensor can be described by each symmetry component. It is standard in the literature to report the percentage anisotropy of a sample as calculated from the minimum and maximum velocities. However, since the elasticity tensor contains much more information than this ratio, it is also customary to plot velocity spheres (or hemispheres as in Fig. 5). The tensor decomposition used here allows for a quantitative description of the entire velocity sphere. In general, the total percentage anisotropy of the elastic tensor for a given sample and given quartz-to-mica ratio is similar but slightly lower than its corresponding AV_p or maximum AV_s [Fig. 9; see also Supporting Information]. The proportion of the total anisotropy of the elastic tensor that has hexagonal symmetry is listed beneath each hemisphere in Figs 5–8, and is illustrated in histogram form in Fig. 9. The sign indicates slow (negative) or fast (positive) symmetry axis (Figs 5–8).

In both natural and synthetic CPO data calculations, the anisotropies of 100 per cent mica compositions are dominantly hexagonal (or transverse isotropic) with a slow symmetry axis (Figs 5–9) and the fast plane aligned with the kinematic x–y plane as would be expected from the single crystal properties of mica (Fig. 3). The 100 per cent mica composition end-member of sample ISR-q has the lowest proportion of hexagonal symmetry (75 per cent) with the remaining 25 per cent of the anisotropy having lower symmetry, which is again attributed to alignment of mica in both S

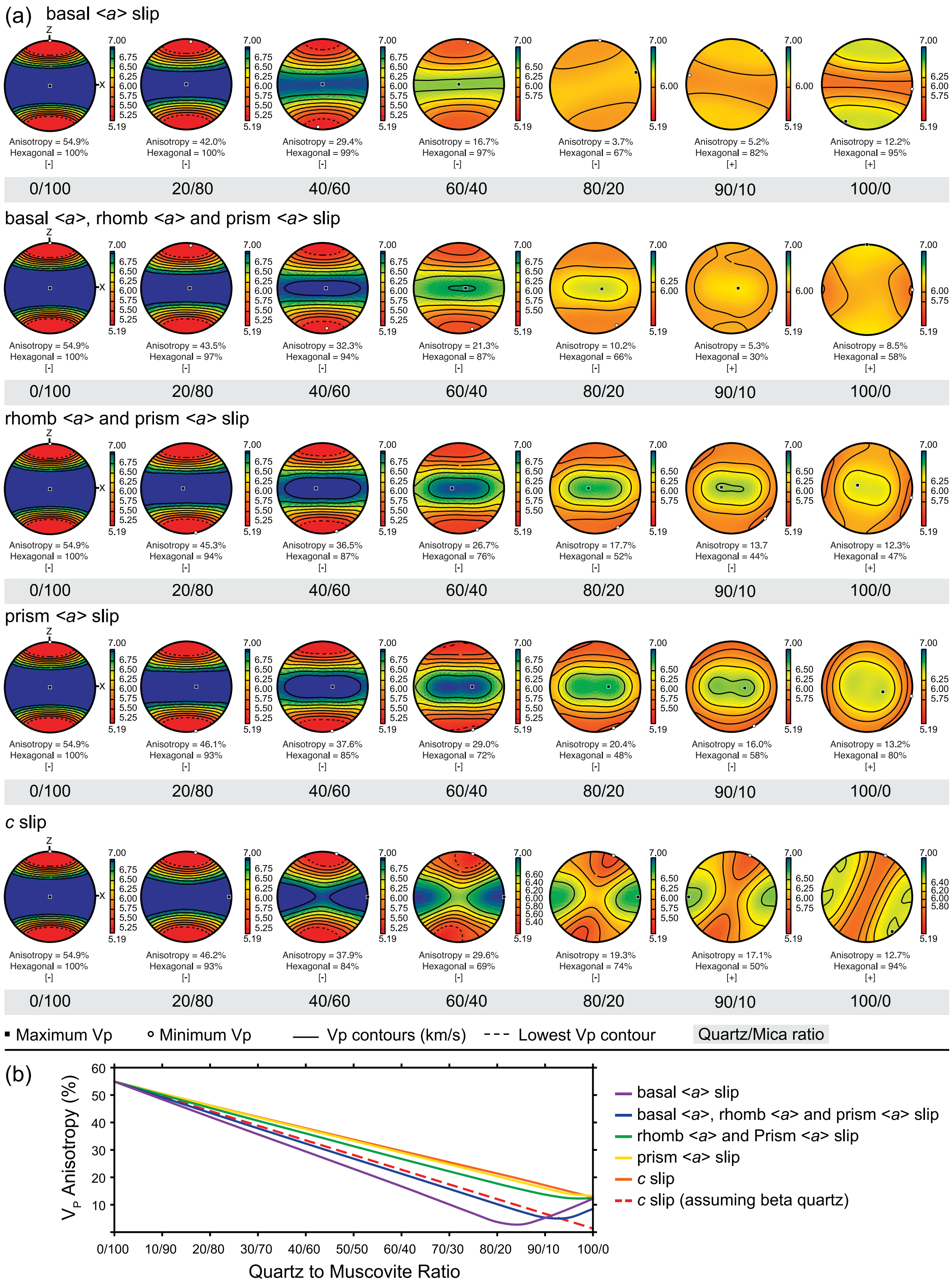

Figure 7. (a) Equal area, lower hemisphere, stereographic projections of V_p calculated for a range of quartz to mica ratios using synthetically generated orientation data. Other definitions as in Fig. 5. (b) AV_p variation with increasing quartz content.

and *C* planes of the composite fabric. Generally, the proportion of hexagonal symmetry of anisotropy initially decreases with decreasing mica content, although it stays above 65 per cent hexagonal down to compositions of 60/40 quartz–mica ratio for all but one of the calculations (Fig. 9). The exception again is sample ISR-q for which the anisotropy is only 39 per cent hexagonal at a 60/40 quartz–mica ratio. With mica contents at 20 per cent to <10 per cent, the hexagonal component generally reaches a minimum,

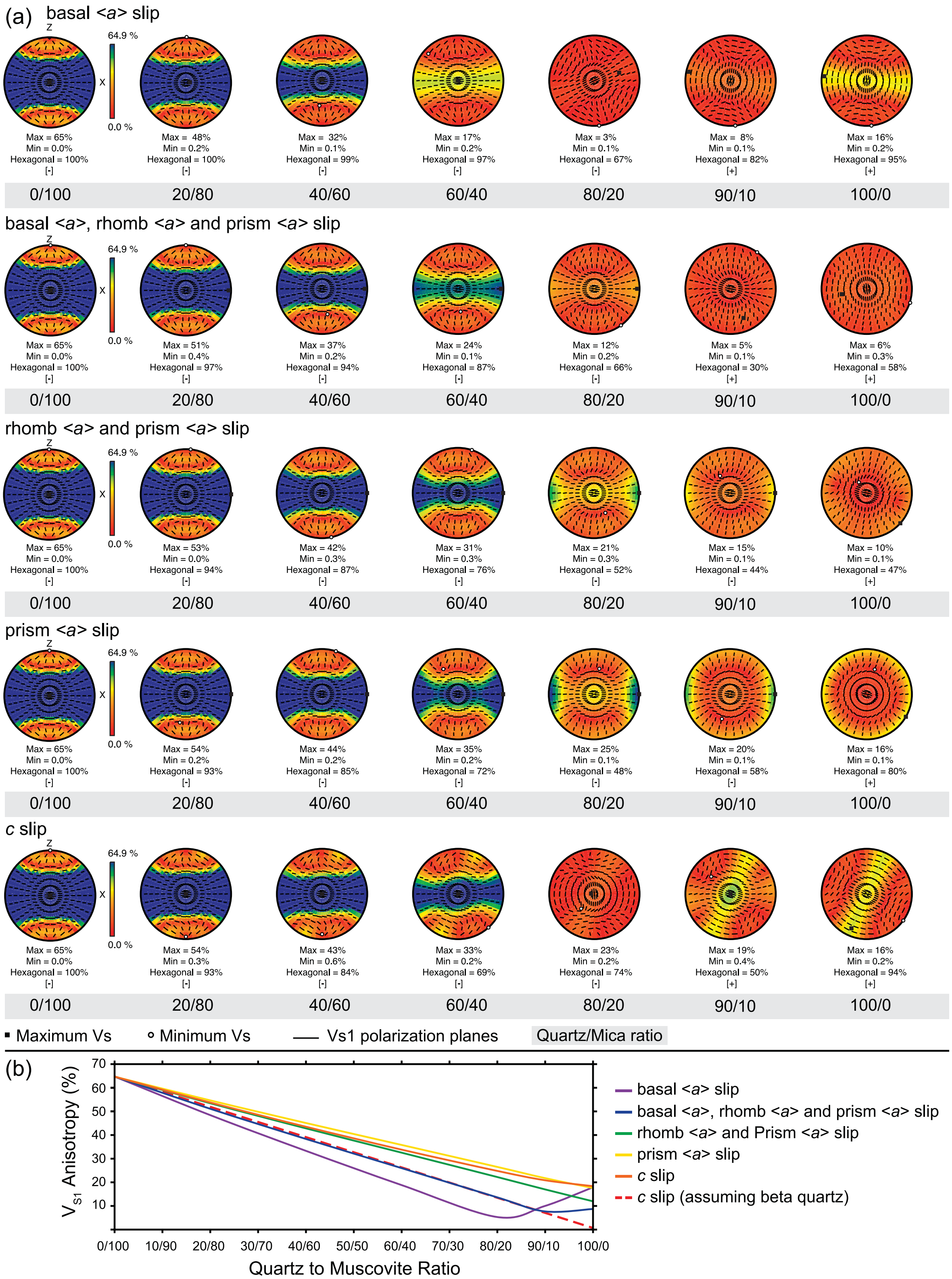

Figure 8. (a) Equal area, lower hemisphere, stereographic projections of AV_s (per cent splitting) calculated for a range of quartz to mica ratios using synthetically generated orientation data. Other definitions as in Fig. 6. (b) Variation of velocity anisotropy of the fast shear wave (AV_S1) with increasing quartz content.

commonly less than 50 per cent and as little as 17 per cent in sample CB-q (Figs 5a and 9A), before increasing slightly at the most quartz-rich compositions. Furthermore, even though the hexagonal component of the anisotropy at the 100 per cent quartz composition may be substantial (e.g. 30–40 per cent in our natural samples and ∼50–95 per cent in the synthetic CPO data sets), the symmetry axis is generally either flipped from slow (as in the mica-rich compositions) to fast or has rotated substantially from the

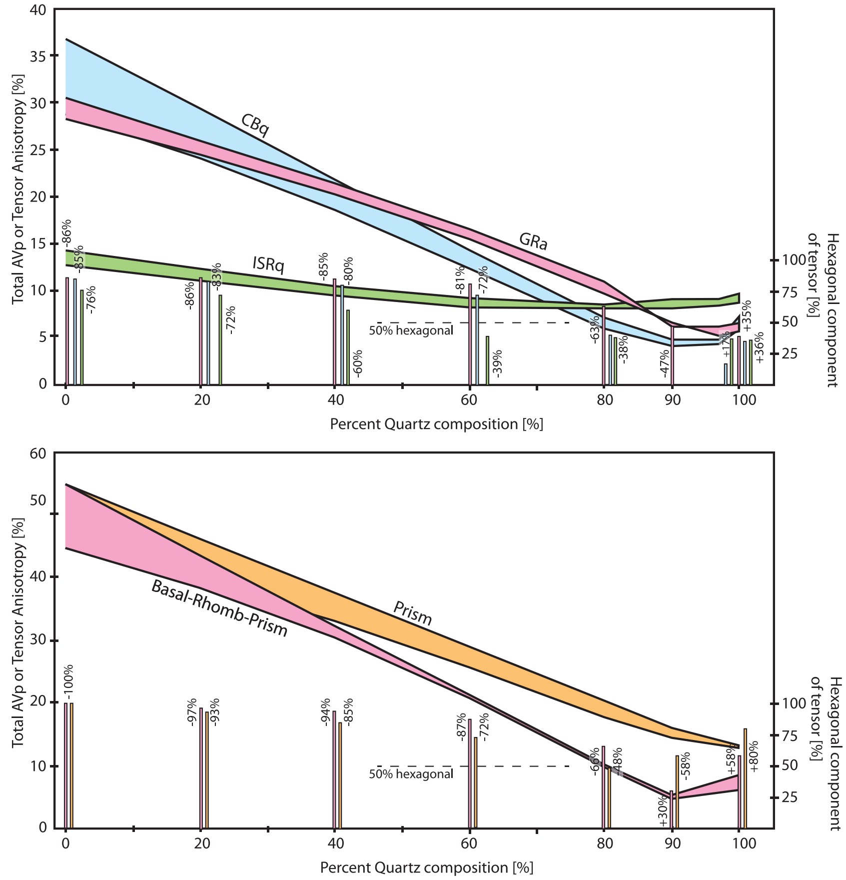

Figure 9. Variation between calculated AV_p (top of filled band) from AnisCh5 (Mainprice 1990) and total anisotropy of the elastic tensor (bottom of filled band) calculated with the code of Browaeys & Chevrot (2004) as a function of increasing quartz content for natural samples (A) and synthetic data sets for basal-rhomb-prism and prism slip (B). Also shown is percentage of the tensor anisotropy that has hexagonal symmetry (histogram bars) using right-hand scale. The sign indicates slow (negative) or fast (positive) symmetry axis.

kinematic x–y plane. In all quartz-rich anisotropy simulations the type of symmetry, the orientation of the symmetry axes, and whether the symmetry axes are fast or slow depend upon which quartz slip systems are active, which are in turn dictated by metamorphic conditions.

CONCLUDING STATEMENTS

Calculation of the variation of AV_p and AV_s over a range of metamorphic conditions in quartz–mica lithologies reveals a mutually destructive relationship between these two phases. Not only does quartz act destructively on the seismic anisotropy produced by aligned mica, as is generally assumed, but the introduction of even minor amounts of aligned mica (as little as 2–4 per cent in low temperature tectonites) can significantly reduce the anisotropy produced by strongly aligned quartz.

These data also suggest that the symmetry of anisotropy is strongly influenced by quartz slip and thus metamorphic grade. There is a minimum threshold proportion of mica (whether a minimum in the anisotropy magnitude curve exists or not) beyond which interpretations of kinematics based on symmetry are not as simple as would be the case for pure aligned mica. Therefore, caution is urged when assuming mica is the sole contributor to either the magnitude or symmetry of anisotropy for polymineralic lithologies. This threshold is not a fixed value but seems to be a function of degree of mineral alignment, deformation temperature, and the identity of other phases. In the present exercise, this threshold is around 20–40 per cent mica. A number of past anisotropy studies have been conducted where this observation may be particularly relevant. For example, Shapiro *et al.* (2004) modelled anisotropy in the Tibetan plateau using 30 per cent mica and 70 per cent assumed isotropic media; Rey *et al.* (1994) have rocks with 35–45 per cent mica and ignore contributions from all other phases. Similar caution may be warranted in assuming that quartz alignment dominates the anisotropy signal (e.g. Lloyd *et al.* 2010) because even small amounts of mica can destructively interfere with quartz-induced anisotropy, particularly at low to moderate temperature.

ACKNOWLEDGMENTS

Funding for this work was in part provided by National Science Foundation grants EAR-0750035 to KM, VS-P, and AS and EAR 0948581 to KM and VS-P. Funding also came from a 2009 Geological Society of America Graduate Student Research Grant to DW, and a grant to DW from the CU Department of Geological Sciences Hartmut Spetzler Fund. Roy Geiss at CU's Nanomaterials Characterization Facility and Susan Swapp at the University of Wyoming's Microscopy Core Facility are gratefully acknowledged for their technical assistance during data collection. Special thanks to G. E. Lloyd and an anonymous reviewer for offering helpful comments to improve the manuscript.

REFERENCES

Aleksandrov, K.S., Alchikov, U.V., Belikov, B.P., Aaslavskii, B.I. & Krupnyi, A.I., 1974. Velocities of elastic waves in minerals at atmospheric pressure and increasing precision of elastic constants by mean of EVM. IZV. *ACD. Sci. USSR Geol. Ser.,* **10,** 15–24.

Browaeys, J.T. & Chevrot, S., 2004. Decomposition of the elastic tensor and geophysical applications, *Geophys. J. Int.,* **159,** 667–678

Chamberlain, K.R., Frost, C.D. & Frost, B.R., 2003. Early Archean to Mesoproterozoic evolution of the Wyoming Province: archean origins to modern lithospheric architecture, *Can. J. Earth Sci.,* **40,** 1357–1374.

Deer, W.A., Howie, R.A. & Zussman, J., 1992. *An Introduction to the Rock-Forming Minerals,* 2nd edn, Pearson Prentice Hall, Harlow, 696pp.

Duebendorfer, E.M., 1988. Evidence for an inverted metamorphic gradient associated with a Precambrian suture, southern Wyoming, *J. Metamorph. Geol.,* **6,** 41–63.

Dumond, G., McLean, N., Williams, M.L., Jercinovic, M.J. & Bowring, S.A., 2008. High-resolution dating of granite petrogenesis and deformation in a lower crustal shear zone: athabasca granulite terrane, western Canadian Shield, *Chem. Geol.,* **254,** 175–196.

Hirth, G. & Tullis, J., 1992. Dislocation creep regimes in quartz aggregates, *J. Struct. Geol.,* **14,** 145–159.

Huang, H., Yao, H. & van der Hilst, R.D., 2010. Radial anisotropy in the crust of SE Tibet and SW China from ambient noise interferometry, *Geophys. Res. Lett.,* **37,** L21310, doi:10.1029/2010GL044981.

Ji, S., Salisbury, M. & Hanmer, S., 1993. Petrofabric, P-wave anisotropy and seismic reflectivity of high-grade tectonites, *Tectonophysics,* **222,** 195–226.

Ji, S., Wang, Q. & Xia, B., 2002. *Handbook of Seismic Properties of Minerals, Rocks and Ores,* Polytechnic International Press, Montreal, ISBN: -553–01032-X.

Karlstrom, K.E. & Houston, R.S., 1984. The Cheyenne Belt: analysis of a Proterozoic suture in southern Wyoming, *Precamb. Res.,* **25,** 415–446.

Khazanehdari, J., Rutter, E.H., Casey, M. & Burlini, L., 1998. The role of crystallographic fabric in the generation of seismic anisotropy and reflectivity of high strain zones in calcite rocks, *J. Struct. Geol.,* **20,** 293–299.

Lister, G.S., 1977. Discussion: crossed girdle c-axis fabrics in quartzites plastically deformed by plane strain and progressive simple shear, *Tectonophysics,* **39,** 51–54.

Lloyd, G.E. & Kendall, J.M., 2005. Petrofabric-derived seismic properties of a mylonitic quartz simple shear zone; implications for seismic reflection profiling, in *Petrophysical Properties of Crystalline Rocks,* Geol. Soc. Lond. Spec. Pub. Vol. 240, pp. 75–94, eds Harvey, P.K., Brewer, T.S., Pezard, P.A. & Petrov, V.A., Geological Society, London.

Lloyd, G.E., Butler, R.W.H., Casey, M. & Mainprice, D., 2009. Mica, Deformation fabrics and the seismic properties of the continental crust, *Earth planet. Sci. Lett.,* **288,** 320–328.

Lloyd, G.E., Law, R.D. & Mainprice, D., 2010. Predicting seismic properties from three-dimensional microstructures: a new look at an old quartzite, in *Continental Tectonics and Mountain Building: The Legacy of Peach and Horne,* Geol. Soc. Lond. Spec. Pub. Vol. 335, pp. 603–622, eds Law, R.D., Butler, R.W.H., Holdsworth, R.E., Krabbendam, M. & Strachan, R.A., Geological Society, London.

Lloyd, G.E., Butler, R.W.H., Casey, M., Tatham, D.J. & Mainprice, D., 2011a. Constraints on the seismic properties of the middle and lower continental crust, in *Deformation Mechanisms, Rheology and Tectonics: Microstructures, Mechanics and Anisotropy,* Geol. Soc. Lond. Spec. Pub. Vol. 360, pp. 7–32, eds Prior, D.J., Rutter, E.H. & Tatham, D.J., Geological Society, London.

Lloyd, G.E., Butler, R.W.H., Casey, M., Tatham, D.J. & Mainprice, D., 2011b. From crystal to crustal: petrofabric-derived seismic modeling of regional tectonics, in *Deformation Mechanisms, Rheology and Tectonics: Microstructures, Mechanics and Anisotropy,* Geol. Soc. Lond. Spec. Pub. Vol. 360, pp. 49–78, eds Prior, D.J., Rutter, E.H. & Tatham, D.J., Geological Society, London.

Mahan, K.H., 2006. Retrograde mica in deep crustal granulites: implications for crustal seismic anisotropy, *Geophys. Res. Lett.,* **33,** L24301, doi:10.1029/2006GL028130.

Mahan, K.H. & Williams, M.L., 2005. Reconstruction of a large deep crustal exposure: implications for the Snowbird Tectonic Zone and early growth of Laurentia, *Geology,* **33,** 385–388.

Mahan, K.H., Goncalves, P., Williams, M.L. & Jercinovic, M.J., 2006. Dating metamorphic reactions and fluid flow: application to exhumation of high-P granulites in a crustal-scale shear zone, western Canadian Shield, *J. Metamorph. Geol.,* **24,** 193–217.

Mainprice, D., 1990. A Fortran program to calculate seismic anisotropy from the lattice preferred orientation of minerals, *Comput. Geosci.,* **16,** 385–393.

Mainprice, D. & Casey, M., 1990. The calculated seismic properties of quartz mylonites with typical fabrics: relationship to kinematics and temperature, *Geophys. J. Int.,* **103,** 599–608.

Mainprice, D. & Humbert, M., 1994. Methods of calculating petrophysical properties from lattice preferred orientation data, *Surv. Geophysics.,* **15,** 575–592.

Mainprice, D.H. & Nicolas, A., 1989. Development of shape and lattice preferred orientations: application to the seismic anisotropy of the lower crust, *J. Struct. Geol.,* **11,** 175–189.

McSkimin, H.J., Andreatch, P. & Thruston, R.N., 1965. Elastic moduli of quartz versus hydrostatic pressure at 25 ˚C and – 195.8 ˚C, *J. appl. Phys.,* **36,** 1624–1632.

McCoy, A.M., Karlstrom, K.E., Shaw, C.A. & Williams, M.L., 2005. The Proterozoic ancestry of the Colorado mineral belt: 1.4 Ga shear zone system in central Colorado, in *The Rocky Mountain Region: An Evolving Lithosphere,* Geophys. Monogr. 154, pp. 71–90, eds Karlstrom, K.E. & Keller, G.R., American Geophysical Union, Washington, DC.

McDonough, D. & Fountain, F., 1993. P-wave anisotropy of mylonitic and infrastructural rocks from a Cordilleran core complex, *Phys. Earth planet. Inter.,* **78,** 319–336.

McNamara, D. & Owens, T., 1993. Azimuthal shear wave anisotropy in the Basin and Range province using Moho Ps converted phases, *J. geophys. Res.,* **98,** 12 003–12 017.

Meissner, R., Rabbel, W. & Kern, H., 2006. Seismic lamination of the lower continental crust, *Tectonophysics,* **416,** 81–99.

Moschetti, M.P., Ritzwoller, M.H., Lin, F. & Yang, Y., 2010. Seismic evidence for widespread western-US deep-crustal deformation caused by extension, *Nature,* **464,** 885–890.

Naus-Thijssen, F.M.J., Goupee, A.J., Vel, S.S. & Johnson, S.E., 2011. The influence of microstructure on seismic wave speed anisotropy in the crust: computational analysis of quartz-muscovite rocks, *Geophys. J. Int.,* **185,** 609–621, doi:10.1111/j.1365246X.2011.04978.x

Passchier, C.A. & Trouw, R.A.J., 2005. *Microtectonics,* Springer, Berlin, ISBN: 3–540-64003–7.

Peng, X. & Humphreys, G., 1997. Moho dip and crustal anisotropy in northwestern Nevada from teleseismic receiver functions, *Bull. seism. Soc. Am.* **87,** 745–754.

Porter, R., Zandt, G. & McQuarrie, N., 2011. Pervasive lower-crustal seismic anisotropy in southern California: evidence for underplated schists and active tectonics, *Lithosphere,* **3,** 201–220.

Tatham, D.J., Lloyd, G.E., Butler, R.W.H. & Casey, M., 2008. Amphibole and lower crustal seismic properties, *Earth planet. Sci. Lett.,* **267,** 118–128.

Rey, P., Fountain, D. & Clement, W., 1994. P wave velocity across a noncoaxial ductile shear zone and its associated strain gradient, *J. geophys. Res.* **99,** 4533–4548.

Roselli, P., Agostinetti, N.P. & Braun, T., 2010. Shear-velocity and anisotropy structure of a retreating extensional forearc (Tuscany, Italy) from receiver functions inversion, *Geophys. J. Int.,* **181,** 545–556, doi:10.1111/j.1365-246X.2010.04520.x.

Schmid, S.M. & Casey, M., 1986. Complete fabric analysis of some commonly observed quartz c-axis patterns, *Geophys. Monograph,* **36,** 263–286.

Schulte-Pelkum, V., Monsalve, G., Sheehan, A., Pandey, M.R., Sapkota, S. & Bilham, R., 2005. Imaging the Indian subcontinent beneath the Himalaya, *Nature,* **435,** 1222–1225.

Shapiro, N.M., Ritzwoller, M.H., Molnar, P. & Levin, V., 2004. Thinning and flow of Tibetan crust constrained by seismic anisotropy, *Science,* **305,** 233–236.

Vaughan, M.T. & Guggenheim, S., 1986. Elasticity of muscovite and its relationship to crystal structure, *J. geophys. Res.,* **91,** 4657–4664.

Zandt, G., Gilbert, H., Owens, T.J., Ducea, M., Saleeby, J. & Jones, C.H., 2004. Active foundering of a continental arc root beneath the southern Sierra Nevada in California, *Nature,* **431,** 41–46.

SUPPORTING INFORMATION

Additional Supporting Information may be found in the online version of this article:

Supplement S1. Elastic tensor files.
Supplement S2. Table with values for AV_p, AV_s, percentage anisotropy of tensor, and percentage hexagonal component of anisotropy of tensor.

Please note: Wiley-Blackwell are not responsible for the content or functionality of any supporting materials supplied by the authors. Any queries (other than missing material) should be directed to the corresponding author for the article.